

Structural and physical properties of transparent conducting, amorphous Zn-doped SnO₂ films

Q. Zhu,¹ Q. Ma,^{2,a)} D. B. Buchholz,¹ R. P. H. Chang,¹ M. J. Bedzyk,¹ and T. O. Mason¹

¹Department of Materials Science and Engineering, Northwestern University, Evanston, Illinois 60208, USA

²DND-CAT, Northwestern Synchrotron Research Center at Advanced Photon Source, Argonne, Illinois 60439, USA

(Received 25 October 2013; accepted 17 December 2013; published online 17 January 2014)

The structural and physical properties of conducting amorphous Zn-doped SnO₂ (*a*-ZTO) films, prepared by pulsed laser deposition, were investigated as functions of oxygen deposition pressure (*p*O₂), composition, and thermal annealing. X-ray scattering and X-ray absorption spectroscopy measurements reveal that at higher *p*O₂, the *a*-ZTO films are highly transparent and have a structural framework similar to that found in crystalline (*c*-), rutile SnO₂ in which the Sn⁴⁺ ion is octahedrally coordinated by 6 O²⁻ ions. The Sn⁴⁺ ion in these films however has a coordination number (CN) smaller by 2%–3% than that in *c*-SnO₂, indicating the presence of oxygen vacancies, which are the likely source of charge carriers. At lower *p*O₂, the *a*-ZTO films show a brownish tint and contain some 4-fold coordinated Sn²⁺ ions. Under no circumstances is the CN around the Zn²⁺ ion larger than 4, and the Zn-O bond is shorter than the Sn-O bond by 0.07 Å. The addition of Zn has no impact on the electroneutrality but improves significantly the thermal stability of the films. Structural changes due to *p*O₂, composition, and thermal annealing account well for the changes in the physical properties of *a*-ZTO films. © 2014 AIP Publishing LLC.

[<http://dx.doi.org/10.1063/1.4861378>]

I. INTRODUCTION

Crystalline transparent conducting oxides (TCOs) have been widely used as transparent electrodes in flat panel displays (FPDs), solar cells, light emitting diodes (LEDs), etc.^{1,2} There is, however, an increasing interest in amorphous (*a*-) TCOs in device applications owing to their advantages over crystalline TCOs. The achievable compositions of amorphous films can extend far beyond their crystalline counterparts, enabling a reduction in the use of expensive elements like indium. Amorphous films, which can be deposited at low temperature on flexible substrates, have good mechanical stabilities under stress^{3–6} and smoother surface morphologies.⁷ They can, therefore, be explored as an enabling technology for flexible electronics.^{7,8} At the same time, *a*-TCOs have comparable electrical and optical properties to their crystalline counterparts.^{5,9}

Amorphous Zn-Sn-O (*a*-ZTO) films, besides being indium-free, have shown superior electrical properties than crystalline films along the ZnO-SnO₂ binary (ZnSnO₃,^{10–12} Zn₂SnO₄,^{10,13,14} Zn-doped SnO₂,¹⁵ or Sn-doped ZnO^{16–18}). Electrical properties of *a*-ZTO films deposited by radio frequency (RF) magnetron sputtering have been examined previously in terms of cation composition and thermal treatment.^{12,15,19} It was found that, for a 10% Zn-doped SnO₂ film, conductivity (σ) increased to ~ 1000 S/cm after vacuum annealing at 300 °C from ~ 250 S/cm for the as-deposited film.¹⁵ However, the structural origin of the changes in physical properties is yet to be clarified. X-ray

absorption spectroscopy techniques²⁰ are well suited for the structural studies of disordered materials. Prior studies have used these techniques to probe the local structures of amorphous material systems such as Zn-In-Sn-O (ZITO),²¹ In-Zn-O (IZO),²² and In-Ga-Zn-O (IGZO),^{23,24} i.e., the bond distances and coordination numbers, around specific cations. However, structure-property relationships have yet to be established. Here, we report a comprehensive study of the physical and structural properties of *a*-ZTO thin films grown by pulsed laser deposition. The local structures of these films were analyzed using X-ray absorption spectroscopy and X-ray scattering techniques, including the changes induced by thermal annealing.

II. EXPERIMENTAL ASPECTS AND METHODS

A. Thin film deposition and property characterization

a-ZTO thin films were deposited on 1 × 1 cm² glass substrates at room temperature by a pulsed laser deposition (PLD) system employing a 248 nm KrF excimer laser. The laser beam was focused using a fused silica lens to a 1 × 2 mm² spot size on the targets, which were rotated at a rate of 5 rpm to prevent localized heating. A dual-target deposition method was employed, where the constituent oxides (ZnO and SnO₂) were used as the targets. The composition of the film was controlled by the deposition time of each target and was later confirmed by energy dispersive X-ray analysis (Hitachi S3400N-II SEM with Oxford INCAx-act Si-drift detector (SDD) EDX). Films with varying Zn/(Zn + Sn) ratios (=0, 0.1, 0.3) were grown under varying oxygen partial pressures (7.5, 10, and 12 mTorr). By controlling the growth rate and time, film thicknesses of 170–280 nm were

^{a)}Author to whom correspondence should be addressed. Electronic mail: q-ma@northwestern.edu

obtained, which were confirmed by optical ellipsometry (J. A. Woollam M2000U). Carrier type, concentration, and mobility of the *a*-ZTO films were measured by Hall effect (Ecopia HMS-3000, Korea) in van der Pauw configuration with a 0.58 T field. Annealing treatments of as-deposited *a*-ZTO90 films were carried out in air at 200 °C, 300 °C, 400 °C, and 450 °C for 1 h to examine changes in their electrical properties and thermal stability. Grazing incidence X-ray diffraction (GIXRD) measurements (Rigaku ATX-G Workstation) were carried out to verify the phase content of the films. In these measurements, the sample surface normal, incident, and scattered wave vectors all lie in the horizontal plane.

B. Structural characterizations using the synchrotron-based X-ray techniques

For structural studies, synchrotron-based X-ray absorption spectroscopy and X-ray scattering measurements were carried out on the *a*-ZTO films at the bending magnet 5-BM-D beamline of the DuPont-Northwestern-Dow-Collaborative Access Team (DND-CAT) at the Advanced Photon Source of Argonne National Laboratory. A Si(111) double-crystal monochromator was used for energy selection with $\Delta E/E = 1.4 \times 10^{-4}$. X-ray absorption spectroscopy techniques²⁰ are well suited for the structural studies of disordered materials. X-ray absorption near edge structure (XANES), typically up to 30 eV above the absorption edge, can provide information on the electronic structure and structural geometry around the absorbing atoms, and extended X-ray absorption fine structure (EXAFS), extending beyond 30 eV above the absorption edge, can reveal coordination number (CN), bond length, and bond spread related to the absorbing atoms.

1. X-ray scattering experiment and data reduction

X-ray scattering measurements were carried out with photon energy of 15 keV for a 550 nm-thick *a*-ZTO90 film ($1 \times 2 \text{ cm}^2$) deposited under a pO_2 of 10 mTorr. A two-mirror (Rh-coated) system vertically focused the X-ray beam to $\sim 200 \mu\text{m}$ at the sample position. The final X-ray beam size was defined by a slit system to $0.1 \times 8 \text{ mm}^2$. The incident intensity was monitored by the X-ray scattered intensity from a thin Kapton foil inserted into the incident beam. A Huber four-circle diffractometer was used to collect the data in a grazing incidence geometry with the X-ray angle of incidence, α , set at 0.5° . Since the critical angle for SnO_2 at 15 keV is 0.2° , we can ignore refraction effects and characterize the X-ray penetration depth (Λ) into the SnO_2 film by its linear absorption coefficient (μ) as $\Lambda = \sin\alpha/\mu = 300 \text{ nm}$. This being sufficiently smaller than the *a*-ZTO90 film thickness (550 nm) ensures that the scattered X-ray intensity primarily originates from the film. To double the data collection efficiency, a square-array 4-element SDD system (Vortex ME4) was mounted on the 2θ arm of the diffractometer with a double-slit system defining two separate 2θ scattering angles with a pair of detecting elements behind each slit. A guard slit was placed halfway between the detectors and the sample to remove stray

scattering. Air scattering was minimized by using evacuated flight paths for both the incident and scattered beams.

The X-ray pulses from the energy-dispersive SDD system were analyzed using the digital X-ray processing electronics (DXP-XMAP, X-ray Instrument Associate, Hayward, CA). The total count rate was sufficiently low that with the peaking time set at $1 \mu\text{s}$, no dead-time corrections were needed. Two regions of interest (ROI) were defined: the higher-energy ROI counted elastic and inelastic scattered photons and a lower-energy ROI counted Zn $K\alpha$ fluorescence photons. The latter was used for a geometrical correction. Processing of the raw data included background removal, data normalization, and a correction for detecting angular offset. The scattering data up to $q_{\text{max}} = 14.5 \text{ \AA}^{-1}$ were used to obtain the pair distribution function (PDF) using the Rad-Gtk + package.²⁵ The elastic and inelastic scattering factors used in the data reduction were obtained from tabulated values.^{26,27}

2. X-ray absorption spectroscopy and data reduction

For X-ray absorption measurements at the Sn L_1 edge, Sn K edge, and Zn K edge, the 2nd crystal of the double-crystal X-ray monochromator was detuned to 60% of its peak intensity to remove higher-order harmonics. The edge energies were calibrated with Sn or Zn foils. Commercial ZnO and SnO_2 powders were used as reference materials. The powder samples were uniformly spread onto Scotch tape, respectively, which was folded a few times to produce a sufficient absorption change at the edge $\Delta\mu t$. The reference samples were measured in transmission mode using ionization chambers (Oxford-Danfysik). The $\Delta\mu t$ employed was ~ 1 for the Zn K edge and ~ 0.5 for the Sn K edge. Thin film samples were measured in fluorescence mode, using one or two Vortex ME4 SDD detectors and the XMAP electronics. The count rate was maintained at $\sim 70\,000$ cps for each SDD detector element. The peaking time was set at $0.3 \mu\text{s}$. Thin film samples were mounted vertically with their surface normal pointing in the horizontal plane and bisecting the $\sim 90^\circ$ angle between the incident beam and detection directions.

The EXAFS data were analyzed using the IFFEFIT software package.²⁸ The EXAFS spectra were fitted with the following equation:

$$\chi(k) = \sum_i \frac{N_i(\theta) |f_i(k)| S_0^2 e^{-2\sigma_i^2 k^2}}{k R_i^2} \times \sin \left[2R_i k + \varphi(k) + \frac{2}{3} C_3 k^3 \right] e^{\frac{-2R_i}{\lambda(k)}}. \quad (1)$$

The passive electron reduction factors S_0^2 of 1.02 for the Sn K-edge and 0.9 for the Zn K-edge were determined from the reference oxides. Note that S_0^2 is used here as a scaling factor only; it was determined from the data measured on the reference materials. $e^{-2\sigma_i^2 k^2}$ is the Debye-Waller factor, where σ is the standard deviation of interatomic distances relative to their mean values R_i . C_3 accounts for the effect of anharmonicity, which is largely absent in the first neighbor interaction in *a*-ZTO films. The structural model was a cluster with rutile structure, centered on the absorbing atom (Sn or Zn).

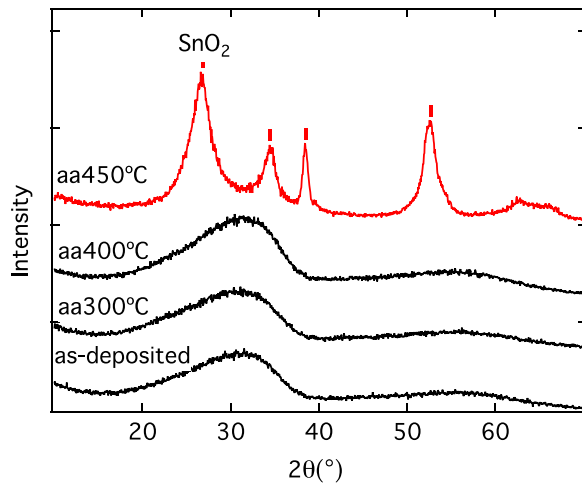


FIG. 1. GIXRD patterns collected at Cu K α ($\lambda = 1.541 \text{ \AA}$) with a 0.5° incident angle from ZTO90 films deposited at pO_2 of 10 mTorr and air-annealed at 300°C , 400°C , and 450°C (red). Starting at $2\theta = 26.6^\circ$, the (hkl) indices of the indicated (vertical bars) rutile crystalline SnO_2 peaks are (110), (011), (020), and (121), consecutively.

XANES simulations were performed on the Sn and Zn K-edge spectra for an a -ZTO90 film using the FDMNES code.²⁹ The finite difference method (FDM) calculation, which utilizes a non-muffin-tin potential set on an equally spaced 3D-grid with a period of 0.25 \AA , is sensitive to structural variations. The simulation can be carried out in a reasonable time for a small cluster that only includes the nearest neighbor. In the simulation, neutral O, Zn, and Sn atoms were assumed.

III. STRUCTURE OF a -ZTO FILMS

As seen in Fig. 1, the GIXRD pattern shows that the a -ZTO90 film crystallizes into rutile SnO_2 after annealing at 450°C , which is not surprising since 90% of the film consists of SnO_2 . Therefore, a direct comparison of the structures of a -ZTO and rutile SnO_2 is in order. Fig. 2 shows the PDF, $G(R)$, around an averaged atom measured on the a -ZTO90 film and the calculated $G(R)$ of crystalline rutile SnO_2 .³⁰ It is seen that the local structure of the a -ZTO90 film ($R < 4 \text{ \AA}$) is quite similar to that of c - SnO_2 . Therefore, c - SnO_2 is an adequate reference for studying the local structures of a -ZTO films. The averaged bond distance $R_{\text{Sn-O}}$ in rutile SnO_2 (*space group*: $P4_2/mnm$, $a = b = 4.7380 \text{ \AA}$, $c = 3.1900 \text{ \AA}$) is 2.0556 \AA with $N = 6$. Two neighbors are at 2.0457 \AA and four are at 2.0606 \AA . The first Sn-Sn distance is at 3.1900 \AA with $N = 2$. The averaged first-shell (M-O) bond distance in the a -ZTO90 film is 2.00 \AA ; 2.8% smaller than $R_{\text{Sn-O}}$ in c - SnO_2 . The second peak in the a -ZTO90 $G(R)$ is poorly resolved and locates a smaller distance as well. The X-ray absorption data will show that this is due in part to a shorter Zn-Sn interaction. The structural differences at large distances may be attributed to disorder and connectivity in a -ZTO90 films.

A. Local structure of a -ZTO films

Fig. 3 shows the Sn K-edge EXAFS spectra and Fourier transforms (FTs) for the as-deposited and post-annealed

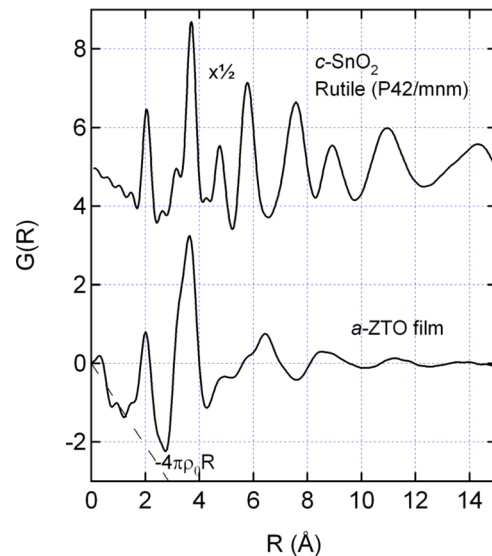


FIG. 2. The pair distribution function $G(R)$ around an average atom measured on the a -ZTO90 film. Also shown is the calculated $G(R)$ based on c - SnO_2 (rutile). Note that the amplitude of the c - SnO_2 data was reduced by a factor of 2. The same q range was used to obtain $G(R)$ in both cases ($q_{\text{max}} = 14.5 \text{ \AA}^{-1}$). The data processing for this PDF analysis is shown in Figs. S4-S7 of Ref. 31.

a -ZTO90 films, as well as that of bulk SnO_2 . For amorphous states (curves a-c), the EXAFS signals die off for $k > 12.5 \text{ \AA}^{-1}$. After 1 h annealing at 450°C , crystallization has occurred as seen in the Sn K-edge EXAFS data (curve d in Fig. 3), and large changes are also observed in the Zn

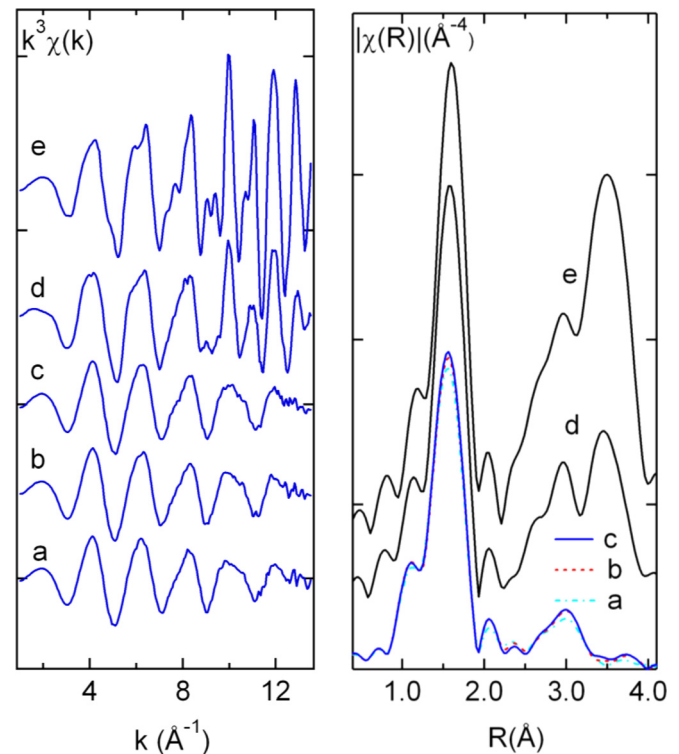


FIG. 3. The k^3 -weighted EXAFS spectra (left panel) and their Fourier transforms (right panel) of Sn K-edges of the ZTO90 film deposited at 10 mTorr (a) and air-annealed at 300°C (b), 400°C (c), 450°C (d), along with that of bulk SnO_2 (e).

K-edge EXAFS data (see curve d of Fig. S1).³¹ Annealing at 300 °C and 400 °C also induces changes in the local structures around Sn in *a*-ZTO90 films, as indicated by the slight increase in the magnitudes of both the first and second peaks in the FTs (curves b and c in Fig. 3).

1. First neighbor structure around Sn

Table I summarizes the bond distances (*R*), coordination numbers (*N*), and Debye-Waller factors of the first coordination shells determined from the EXAFS analyses. The results from the Sn K-edge EXAFS data were obtained with *k* range from 2.4 to 9.5 Å⁻¹, while the Zn K edge EXAFS data were analyzed up to 11.6 Å⁻¹. The rationale for using the short data range in the case of the Sn K edge is discussed in detail below. From Table I, the coordination numbers around Sn are smaller in *a*-SnO₂ and *a*-ZTO films than that in bulk SnO₂. This is particularly evident in the case of the *a*-ZTO70 film, which exhibited a light brown hue. Once crystallized, both *N* and *R* around Sn in the 450 °C-annealed ZTO90 film becomes indistinguishable from those in bulk SnO₂. The only difference is a larger σ^2 value. The Sn-O bonds in *a*-ZTO films are consistently shorter than that of the crystalline phase, albeit within the margin of error (± 0.01 Å). The σ^2 values for both the Sn-O and Zn-O bonds are nearly twice as large as those in the crystalline phases, indicating a disordered first coordination shell in the *a*-ZTO films. The small increases in the FT magnitudes (Fig. 3) induced by annealing at 300 °C and 400 °C appear to be accounted for by the reduction in σ^2 , likely suggesting occurrence of ordering.

There is also evidence, although subtle, that σ^2 is not the only structural parameter that is affected by annealing at 300 °C and 400 °C. It was observed that in the cases of 300 °C- and 400 °C-annealed ZTO90 films as well as the *a*-SnO₂ film, *N* around Sn decreased monotonically by as much as 5% when increasing the EXAFS data range or increasing the upper limit (*k*_{max}) from 9.5 to 12.4 Å⁻¹ used in the analyses. Meanwhile, the figure of merit for the fittings deteriorates by nearly 4-fold. In contrast, such a relation is much weaker, if any, for the as-prepared ZTO film (see Fig. S2 in Ref. 31). It has been

TABLE I. EXAFS-determined structural parameters of the first coordination shells for *a*-ZTO films deposited at pO₂ = 10 mTorr. Note: Error bar is ± 0.01 Å for *R* and ± 0.1 for *N* obtained at the Sn K edge. Error bar is ± 0.01 Å for *R* and ± 0.2 for *N* obtained at the Zn K edge. The film data from *k* = 2.45 to 9.46 Å⁻¹ for Sn K edge and from *k* = 2.45 to 11.61 Å⁻¹ for Zn K edge were used, respectively. For the Sn K edge data, the error bar for *N* is ± 0.2 up to 11.6 Å⁻¹ and is ± 0.3 at *k* = 12.4 Å⁻¹.

Samples	<i>R</i> (Å)		<i>N</i>		$\sigma^2 (\times 10^{-3} \text{ \AA}^2)$	
	Sn-O	Zn-O	O _{Sn}	O _{Zn}	Sn-O	Zn-O
<i>c</i> -SnO ₂ /ZnO	2.06	1.96	6	4	2.9	4.3
<i>a</i> -SnO ₂	2.05	...	5.8	...	6.2	...
<i>a</i> -ZnO	...	1.97	...	3.7	...	5.2
<i>a</i> -ZTO70	2.04	1.98	5.4	2.9	5.8	6.5
<i>a</i> -ZTO90	2.05	1.98	5.7	3.7	6.1	7.8
(300 °C)	2.05	1.98	5.8	3.7	5.9	7.3
(400 °C)	2.05	1.97	5.8	3.6	5.8	7.2
(450 °C)	2.06	1.94	6.0	2.9	3.8	7.3

recently shown that in the case of *a*-SnO₂ films, such a peculiar behavior is caused by the existence of two Sn-O bond distances in the first coordination shell.³² The *k*_{max}-dependence is removed when the data are modeled by a double-shell model (i.e., two bond lengths). Fig. 4 displays as an example of the fittings obtained under various conditions for the 300 °C-annealed ZTO90 film. For a single shell model with *k*_{max} = 12.4 Å⁻¹, the fitting is poor in the high *k* range but is much improved by the double-shell model. The weight-averaged $R = (N_1R_1 + N_2R_2)/(N_1 + N_2) = 2.05$ Å and $N = (N_1 + N_2) = 5.9$ are similar to the values obtained using *k*_{max} = 9.5 Å⁻¹ (Table I). Therefore, a single-shell model may adequately reveal the local structures around Sn when the EXAFS data are analyzed over a short *k* range, say 2.5–9.5 Å⁻¹.

A direct comparison of the experimental data is given in Fig. 5 to further illustrate this point, where the first shell EXAFS spectra of the Sn K edge are presented. The lower graph in Fig. 5 shows the difference EXAFS spectra obtained by subtracting the data of the as-deposited film from those of the 300 °C- and 400 °C-annealed films, respectively. It is seen that upon 300 °C annealing, a beating node develops around 9 Å⁻¹ due to the development of two Sn-O bond distances in the first shell around Sn, which requires the double-shell modeling as described above. Yet, the effect is weak and can be approximated by a reduction in σ^2 for the short data range (*k*_{max} = 9.5 Å⁻¹).

As pointed out previously, upon annealing at 400 °C, the FT magnitude further increased (see Fig. 3). The change can also be seen in the first shell EXAFS data when compared to the 300 °C-annealed data (the upper graph of Fig. 5). However, this change is opposite to that seen when going from the as-deposited film to the 300 °C-annealed film.

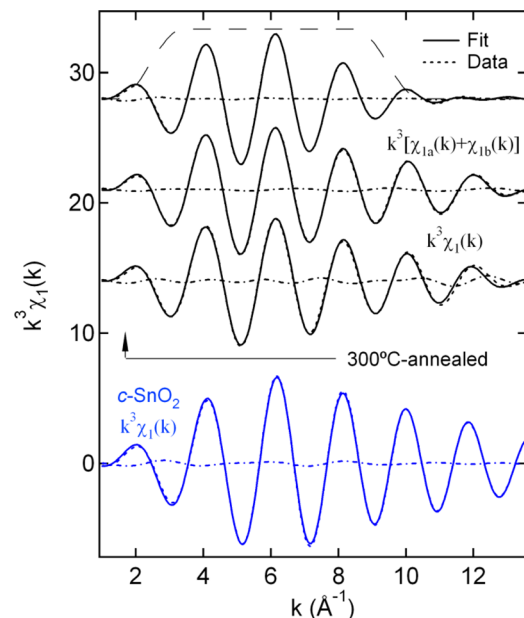


FIG. 4. Fitting results obtained of the first coordination shell $\chi_1(k)$ for the 300 °C-annealed *a*-ZTO90 film. The data were fitted with single or double shells for which *k* = 2.45–12.4 Å⁻¹ and on the top, a single-shell fitting for which *k* = 2.45–9.46 Å⁻¹ (indicated by the window function) is shown as well. A fitting result obtained assuming a single shell for *c*-SnO₂ is also presented on the bottom as a benchmark.

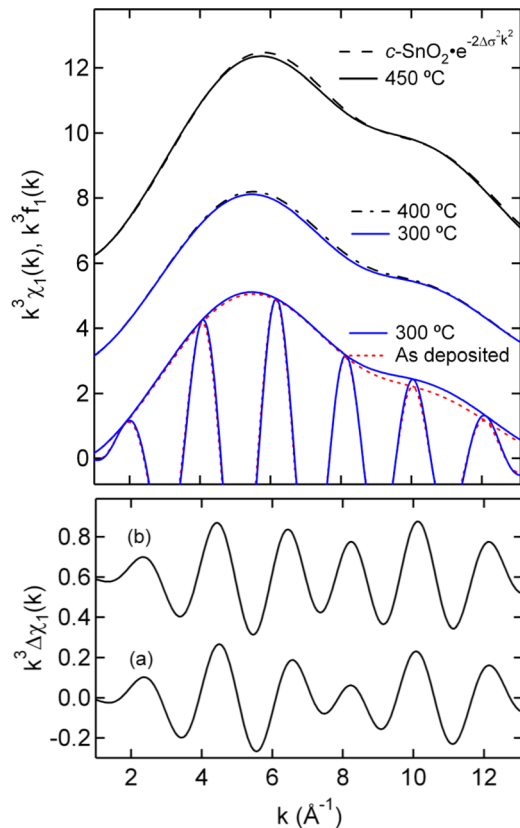


FIG. 5. Upper: comparison of the first shell oscillations $\chi(k)$ and amplitudes $f(k)$ extracted from the EXAFS spectra measured on as-deposited *a*-ZTO films and films annealed for 1-h at various temperatures in air. Also shown for comparison are the *c*-SnO₂ data multiplied by $\exp(-2\Delta\sigma^2 k^2)$ with $\Delta\sigma^2 = \sigma_{c\text{-SnO}_2}^2 - \sigma_{450^\circ\text{C}}^2 = 0.0009 \text{ \AA}^2$ (see Table I). For clarity, only the amplitudes are shown in certain cases. Lower: differences $\Delta\chi(k)$ of the first shell oscillations; (a) 300 °C—as deposited and (b) 400 °C—as deposited.

When compared against the as-deposited film, the beating node around 9 \AA^{-1} is much less prominent after annealing at 400 °C (the lower graph of Fig. 5). In order to better understand this change, the *c*-SnO₂ data are multiplied by a reduced Debye-Waller factor, $e^{-2\Delta\sigma^2 k^2}$, and are overlaid on the 450 °C-annealed data, as shown in the upper graph of Fig. 5. Interestingly, the differences seen in this comparison are very similar to those seen in the comparison between the 300 °C and 400 °C annealed data. It seems that the change from 300 °C annealing to 400 °C annealing is in the same direction as from 450 °C annealed to *c*-SnO₂. With further annealing, the two well separated Sn-O bonds in the first shell, developed by 300 °C annealing, *start* to merge; the film structure evolves in the direction of crystallization.

2. First neighbor structure around Zn

A single shell model appears to be adequate for the first coordination around Zn in *a*-ZTO films. As seen in Table I, $R_{\text{Zn-O}} = 1.98 \text{ \AA}$ and $N \sim 4$. Similar values were reported for ZITO,²¹ IZO,²² and IGZO.^{23,24} After annealing at 450 °C, the film crystallized, and both R and N decreased.

In order to better understand the geometry around Zn, XANES calculations were carried out and the results are shown in Fig. 6 together with reference spectra. It can be seen in Fig. 6(b) that the Sn K-edge XANES of the *a*-ZTO90

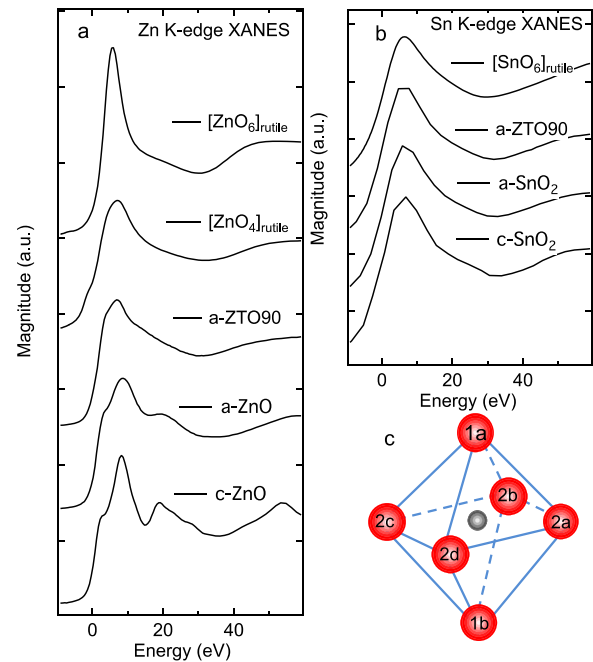


FIG. 6. (a) Comparisons of two FDM computing results based on rutile $[\text{ZnO}_6]$ and $[\text{ZnO}_4]$ with the Zn K-edge XANES of *a*-ZTO90 film, *a*-ZnO, and *c*-ZnO. The result for the $[\text{ZnO}_4]$ best fit is a combination of disordered planar and triangle pyramidal structures (see text). (b) Comparisons of a FDM calculation result $[\text{SnO}_6]$ with the Sn K-edge XANES of *a*-ZTO90 film, *a*-SnO₂, and *c*-SnO₂. (c) The local structure model found in rutile SnO₂ used in the FDM calculations for both Sn and Zn K-edges. The metal atom (Zn or Sn) was placed in the center (grey ball), and oxygen atoms (red symbols) are labeled to facilitate the discussion; see the main text.

film is similar to that of *a*-SnO₂ or *c*-SnO₂, and can be well reproduced by assuming a simple octahedral unit derived from *c*-SnO₂ (Fig. 6(c)). Therefore, the Sn K-edge XANES is dominated by the first neighbor interaction. For the Zn K-edge, however, the XANES spectrum deviates markedly from that of wurtzite ZnO or *a*-ZnO (Fig. 6(a)). It in fact bears resemblance to that of *a*-SnO₂, indicating that Zn likely resides in a rutile-like environment. Therefore, the octahedral model was used as well for the Zn K-edge XANES calculations. However, $[\text{ZnO}_6]_{\text{rutile}}$ does not match the experimental data (Fig. 6(a)). To obtain a better match, both a reduction in the CN and a lower symmetry are required. In addition, some disorder was artificially created. The $[\text{ZnO}_4]_{\text{rutile}}$ model that provides the best match is a combination of disordered planar (with 1a, 1b removed) and triangle pyramidal (with 1a, 2a removed) structures. This exercise implies that local structures around Zn in *a*-ZTO90 films are dominated by large distortion.

B. Second neighbor structures around Zn and Sn

As seen in Fig. 2, the second peak of the *a*-ZTO PDF is poorly resolved. In order to gain the element-specific information under the peak, the EXAFS data analyses including the second shells (Fig. S3 in Ref. 31) were carried out. Assuming no phase separation in *a*-ZTO films, the Zn-Sn interaction should dominate the second shell around Zn. Given the low Zn content, the Sn-Sn interaction should dominate the second shell around Sn. The fitting results (Table

S1 in Ref. 31) show that the Zn-Sn interaction is at 3.08 Å and that the Sn-Sn interaction is at 3.26 Å for *a*-ZTO90 films.

For the 450 °C-annealed ZTO film, the local structure around Sn is similar to that in *c*-SnO₂, while the local structure around Zn undergoes a large change (Table I). The Zn-Sn distance is 3.12 Å, which is longer by 0.04 Å than that in *a*-ZTO90 and is closer to the first Sn-Sn distance in *c*-SnO₂. It is speculated that crystallization asserts a long range force that displaces Sn away from Zn and that in the course of such a structural rearrangement, Zn loses oxygen ($N=3$). The oxygen gain around Sn may be at the expense of the oxygen loss around Zn, suggesting oxygen vacancy migration from Sn to Zn. This may be understood in terms of the relative bond strength: the Sn-O bond is stronger than that of the Zn-O bond.³³

IV. STRUCTURE-PROPERTY RELATIONSHIPS IN *a*-ZTO FILMS

From the results presented above, it is clear that the local structures around Sn in the *a*-ZTO film (10 mTorr) resemble that of *c*-SnO₂ and are very similar to that of *a*-SnO₂. The smaller coordination number around Sn suggests that the oxygen vacancies (V_O) are present in *a*-ZTO films, on the order of 10^{21} cm^{-3} , and are likely the source of carriers. The difference between this estimate and the much smaller carrier concentration of $\sim 10^{19}\text{--}10^{20} \text{ cm}^{-3}$, as measured by Hall effect measurements, indicates the prevalence of neutral oxygen vacancies (V_O^\times) over charged vacancies (V_O^\bullet).

Despite of large distortion in the local structure around Zn, Zn ions behave as if they are “substitutional” in the 10-mTorr *a*-ZTO90 films. The distortion is likely attributable to the substitution of a large Sn ion with a small Zn ion and to the fact that the Zn ion has a much smaller coordination

number. Unlike *a*-SnO₂ films deposited under similar conditions, in which the first shell consists of two distinguishable bond distances,³² the first shell in the as-prepared *a*-ZTO90 film is better described by a single bond distance. Therefore, doping of Zn in SnO₂ induces bond disorder. Thermal annealing experiments show that *a*-ZTO90 crystallized between 400 °C and 450 °C (Fig. 1), whereas the *a*-ZTO70 films annealed at 600 °C were still amorphous (not shown). In comparison, the *a*-SnO₂ film crystallizes at approximately 300 °C.¹⁵ Therefore, the addition of Zn significantly improves the thermal stability of the films by increasing the crystallization temperature (T_{cryst}). Such enhancement in T_{cryst} , a macroscopic property, also suggests no phase separation in these *a*-ZTO films. Given the differences in the bond distances between the Zn-O bond or the Sn-O bond, there exists strain ϵ ($=\Delta R/R$) in *a*-ZTO films that is compressive in nature globally by -0.5% ³⁴ and tensile locally around Zn ions by 3.4%. The strain may reduce the lattice thermal vibrations and increase the energy barrier towards crystallization ($e^{-\Delta E/kT}$, $\Delta E = \Delta E_{a-SnO_2} + \Delta E_{strain}$).

Fig. 7 shows the electrical properties of the *a*-ZTO films as functions of (a) composition, (b) oxygen deposition pressure (pO_2), and (c) thermal annealing. With $pO_2 \geq 10$ mTorr (Figs. 7(a) and 7(b)), the carrier concentrations of the *a*-ZTO films are in the range of $\sim 10^{19}\text{--}10^{20} \text{ cm}^{-3}$, and the mobility varies from 12 to 22 cm^2/Vs , which are comparable to the values of polycrystalline SnO₂ films.³⁵

A. Composition effect on the electrical properties

The data in Fig. 7(a) (all films grown at $pO_2 = 10$ mTorr) provide important information about the role of Zn in carrier generation and transport. At 10% doping, for example, the Zn cation concentration would be on the order of $3 \times 10^{21}/\text{cm}^3$, which is an order of magnitude larger than the carrier content

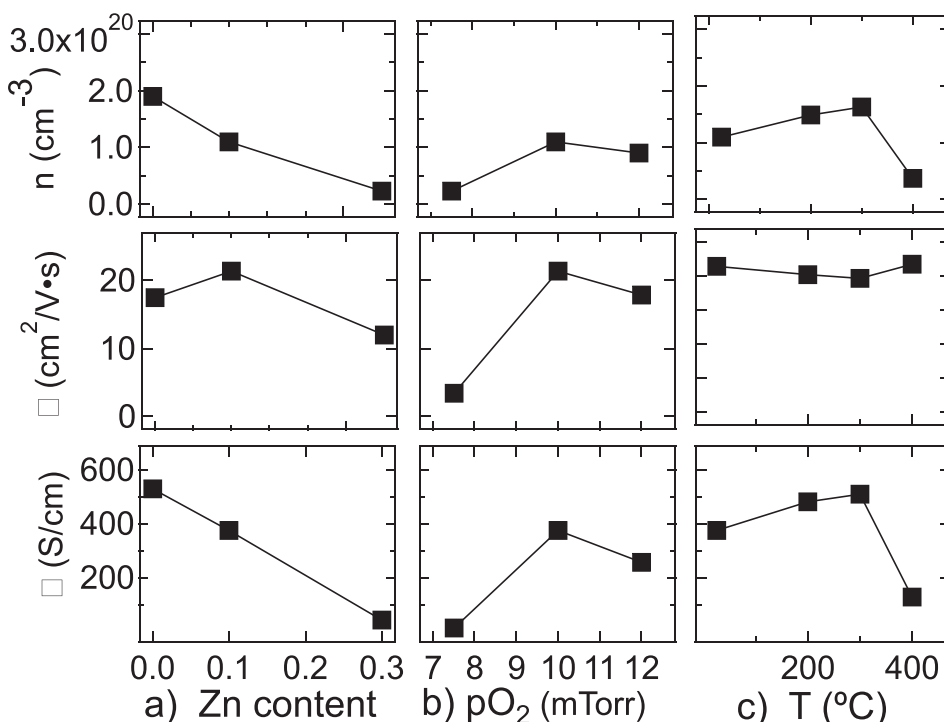


FIG. 7. (a) Changes of conductivity σ (S/cm), carrier concentration n (cm^{-3}), and Hall mobility μ (cm^2/Vs) of a) *a*-ZTO films as a function of Zn content (all deposited at 10 mTorr); (b) *a*-ZTO90 films as a function of deposition pO_2 ; (c) *a*-ZTO90 films as a function of air-annealing temperature. The film annealed at 450 °C was completely insulating and is not shown.

of $\sim 10^{20}/\text{cm}^3$. Furthermore, the decrease in carrier content from undoped $a\text{-SnO}_2$ to $a\text{-ZTO90}$ is relatively modest, i.e., $\sim 50\%$. If Zn were acting as an unbound acceptor dopant (i.e., Zn_{Sn}'') at such a large concentration, as proposed by Liu *et al.*³⁶ for Zn-doped SnO_2 nanorods, the electron population should be decreased by orders of magnitude. Instead there is a much less dramatic, and monotonic, decrease in carrier content and conductivity with increasing Zn-level in Fig. 7(a). This requires that the Zn-dopant is accommodated by self-compensating defects such as $(\text{Zn}_{\text{Sn}}''\text{V}_{\text{O}}^{\bullet})^x$ or in charge-neutral structural units (e.g., distorted $[\text{ZnO}_4]^0$). Either case implies negligible contribution from Zn doping to the overall electroneutrality. With 30% Zn doping, the film showed a light brown hue (likely due to the formation of Sn^{2+} , as described below in Sec. IV B). With $[\text{ZnO}_4]$ and/or $[\text{SnO}_4]$ formation in place of the “host” $[\text{SnO}_6]$, disorder (structural and/or compositional) may be expected in $a\text{-ZTO}$ films. The disorder may increase localization, leading to an increase in neutral $\text{V}_{\text{O}}^{\times}$ at the expense of $\text{V}_{\text{O}}^{\bullet}$ donors. The same disorder most likely accounts for the ultimate decrease in mobility (between 10% and 30% Zn substitution). Robertson³⁷ found that similar localization/compositional disorder was responsible for diminishing the transport properties of several In_2O_3 -based amorphous systems.

The initial increase in mobility with doping between undoped $a\text{-SnO}_2$ and 10% doped $a\text{-ZTO}$ in Fig. 7(a), which is also seen for similar carrier concentrations in the report (Fig. 4) on $a\text{-ZTO}$ films prepared by RF sputtering by Ko *et al.*,¹⁵ may be unique amongst $a\text{-TCOs}$. One explanation is an increase in ns-orbital overlap owing to the smaller Zn-Sn distance vs. that of the Sn-Sn distance (see Sec. III B).³⁸ Another explanation is our finding that Zn addition diminishes the anisotropy observed in the $a\text{-SnO}_2$ film (see Sec. III A 1) and increases thermal stability. At higher Zn-doping levels, however, compositional disorder dominates (as in most $a\text{-TCOs}$), and the mobility declines.

B. Effect of oxygen partial pressure on the electrical properties

The deposition oxygen pressure is a crucial factor affecting the electrical properties of $a\text{-ZTO}$ films, as seen in Fig. 7(b). At a $p\text{O}_2$ of 10 mTorr, optimal carrier concentration n , mobility μ , and electrical conductivity σ were obtained. These decreased slightly at a $p\text{O}_2$ of 12 mTorr, which is likely caused by a reduction in the oxygen vacancy content at the higher $p\text{O}_2$. The film deposited at $p\text{O}_2$ of 7.5 mTorr, however, behaved quite differently and exhibited a brownish hue. Moreover, the electrical properties deteriorated significantly, which is believed to be due to the reduction from Sn^{4+} to Sn^{2+} , as suggested for $a\text{-ZITO}$ films.²¹

Fig. 8 compares the first derivatives of the Sn L_1 edge XANES measured on the $a\text{-ZTO90}$ films, deposited at 10 mTorr and 7.5 mTorr, and bulk SnO_2 . Main peaks corresponding to Sn^{4+} were observed in both films and bulk SnO_2 . However, for the 7.5-mTorr $a\text{-ZTO90}$ films, a separate peak appeared at -3.2eV to the absorption edge for Sn^{4+} . This energy difference is comparable to that of the Sn L_1 absorption edges reported for SnO and SnO_2 .³⁹ This supports

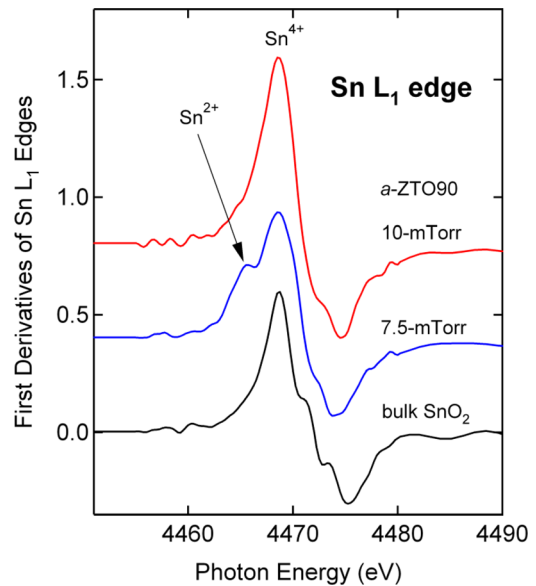


FIG. 8. Comparison of the first derivatives of the Sn L_1 edges measured on the $a\text{-ZTO90}$ films, deposited at 10 mTorr and 7.5 mTorr, and bulk SnO_2 .

the conclusion that the brownish tint observed in this film is due to the formation of Sn^{2+} (up to 30%, as estimated from the peak ratio). In bulk SnO , Sn is coordinated by 4 oxygen,⁴⁰ and is likely to be the same for the Sn^{2+} ions in this $a\text{-ZTO}$ film; the small coordination number around Sn obtained for the $a\text{-ZTO70}$ film (Table I), which was similarly brownish in color, substantiates this conclusion. The drop in n to $\sim 10^{19}\text{cm}^{-3}$ (low carrier concentration regime) may be attributable to the considerable replacement of host Sn^{4+} species (and associated $\text{V}_{\text{O}}^{\bullet}$ donors). The presence of a large amount of Sn^{2+} , regardless of its local environment, indicates that the structure has departed drastically from that of $a\text{-SnO}_2$; the resulting disorder (structural, compositional) accounts for the parallel dramatic drop in mobility.

C. Effect of thermal annealing on the electrical properties

The effect of annealing on the electrical properties of the $a\text{-ZTO90}$ films deposited under $p\text{O}_2$ of 10 mTorr is shown in Fig. 7(c) as a function of temperature. It is seen that σ increases with annealing temperature up to 300°C by $\sim 46\%$ to 510S/cm , after which σ decreases dramatically. The changes in the carrier concentration are primarily responsible for the changes in σ , since μ varies within 10% (the error bar is $\pm 4\%$). After annealing at 400°C , both n and σ decreased. Crystalline SnO_2 peaks were identified in the film annealed at 450°C (Fig. 1), which was so resistive that conductivities could not be reliably measured.

For the 450°C -annealed film, the first shell around Sn is identical to that in $c\text{-SnO}_2$ in terms of the bond distance and coordination number (Table I), while the σ^2 value is still 30% larger than that in $c\text{-SnO}_2$. As shown in Fig. 3, the crystallinity is likely poor and significant disorder remains in this film. Moreover, the N around Zn decreased (~ 3) and so does the Zn-O bond distance. Therefore, the insulating behavior of this film is a direct consequence of the loss of carrier concentration and its poor crystallinity.

Upon annealing at 300 °C, the first coordination shell around Sn separates more prominently into two subshells. This is indicative of structural relaxation from a state strained by Zn doping to a state similar to that in α -SnO₂, at least around Sn cations. This is consistent with the fact that undoped α -SnO₂ has higher carrier (donor) content than Zn-doped films (Fig. 7(a)). It seems reasonable that V_{O}^{\times} donors are formed at the expense of V_{O}^{\times} due to the structural relaxation.

With further annealing at 400 °C, the higher EXAFS magnitude suggests that the local structure of the 400 °C film is evolving in the direction of crystallization, in spite of being “X-ray amorphous” (Fig. 1). The “incipient” stage of crystallization at this annealing temperature is believed to be responsible for the relatively steep reduction in carrier concentration and electrical conductivity (Fig. 7(c)).

V. CONCLUSIONS

The structural and physical properties of conducting amorphous Zn-doped SnO₂ (α -ZTO) films, prepared by pulsed laser deposition, were investigated as functions of oxygen deposition pressure (p_{O_2}), composition, and thermal annealing. The results reveal that at higher p_{O_2} , the α -ZTO films are highly transparent and have a structural framework similar to that found in crystalline (c -), rutile SnO₂ in which the Sn⁴⁺ ion is octahedrally coordinated by 6 O²⁻ ions. The Sn⁴⁺ ion in these films however has a CN smaller by 2%-3% than that in c -SnO₂, indicating the presence of oxygen vacancies, which are the likely source of charge carriers. At lower p_{O_2} , the α -ZTO films show a brownish tint and contain some Sn²⁺ ions that are likely 4-fold coordinated. Zn ions appear to be “substitutional” (i.e., they are in a rutile-like cation environment). However, the Zn-O bond is shorter than the Sn-O bond by 0.07 Å and under no circumstances the CN around the Zn²⁺ ion is larger than 4. The addition of Zn has no impact on the electroneutrality but significantly improves the thermal stability of the α -ZTO films, likely due to the strained structure as a result of the Zn doping.

Except for the initial increase in mobility with 10% Zn doping, attributed to improved structural homogeneity vis-à-vis undoped α -SnO₂, the electrical properties of α -ZTO films tend to decrease with increasing Zn content and/or formation of the Sn²⁺ ions due to formation of [ZnO₄] and/or [SnO₄], leading to disorder, structural, and/or compositional. Upon thermal annealing, changes in the local structures are observed. The change in electrical conductivity, which improves noticeably when annealed at \leq 300 °C, can be explained by structural relaxation (more V_{O}^{\times} formed at the expense of V_{O}^{\times}). The EXAFS results for the crystallized, insulating film suggest oxygen vacancy transfer from Sn to Zn, with a concomitant loss of V_{O}^{\times} donors. Upon annealing at 400 °C, it is speculated that the film, although amorphous by X-ray diffraction, shows evidence for incipient crystallization, which adversely affects the transport properties of the film.

ACKNOWLEDGMENTS

Film growth, electrical characterization, GIXRD, and X-ray absorption measurements were supported by the NSF

funded Materials Research Science and Engineering Center (MRSEC) at Northwestern under Grant No. DMR-1121262. Optical characterization and structural analysis was supported by the ANSER Center, an Energy Frontier Research Center funded by the U.S. Department of Energy, Office of Basic Energy Sciences, under Award No. DE-SC0001059. GIXRD measurements used the NU-MRSEC supported X-ray Diffraction Facility. X-ray absorption and scattering measurements were conducted at the DND-CAT at the Advanced Photon Source (APS). DND-CAT is supported by the NU Office of Research, E.I. DuPont de Nemours & Co., and The Dow Chemical Company. Use of the APS was supported by the U. S. Department of Energy, Office of Science, Office of Basic Energy Sciences, under Contract No. DE-AC02-06CH11357.

- ¹E. Fortunato, D. Ginley, H. Hosono, and D. C. Paine, *MRS Bull.* **32**, 242 (2007).
- ²D. S. Ginley, H. Hosono, and D. C. Paine, in *Handbook of Transparent Conductors*, edited by David S. Ginley (Springer, New York, 2010).
- ³T. Kamiya and H. Hosono, *NPG Asia Mater.* **2**(1), 15 (2010).
- ⁴J. Liu, D. B. Buchholz, R. P. Chang, A. Facchetti, and T. J. Marks, *Adv. Mater.* **22**(21), 2333 (2010).
- ⁵T. Minami, S. Takata, H. Sato, and H. Sonohara, *J. Vac. Sci. Technol., A* **13**(3), 1095 (1995).
- ⁶M. P. Taylor, D. W. Readey, M. F. A. M. van Hest, C. W. Teplin, J. L. Alleman, M. S. Dabney, L. M. Gedvilas, B. M. Keyes, B. To, J. D. Perkins, and D. S. Ginley, *Adv. Funct. Mater.* **18**(20), 3169 (2008).
- ⁷H.-M. Kim, S.-K. Jung, J.-S. Ahn, Y.-J. Kang, and K.-C. Je, *Jpn. J. Appl. Phys., Part 1* **42**(1), 223 (2003).
- ⁸H. Hara, T. Hanada, T. Shiro, and T. Yatabe, *J. Vac. Sci. Technol., A* **22**(4), 1726 (2004).
- ⁹C. A. Hoel, T. O. Mason, J.-F. Gaillard, and K. R. Poepplmeier, *Chem. Mater.* **22**(12), 3569 (2010).
- ¹⁰T. Minami, H. Sonohara, S. Takata, and H. Sato, *Jpn. J. Appl. Phys., Part 2* **33**(12A), L1693 (1994).
- ¹¹M. G. McDowell, R. J. Sanderson, and I. G. Hill, *Appl. Phys. Lett.* **92**(1), 013502 (2008).
- ¹²J. D. Perkins, J. A. del Cueto, J. L. Alleman, C. Warmingsingh, B. M. Keyes, L. M. Gedvilas, P. A. Parilla, B. To, D. W. Readey, and D. S. Ginley, *Thin Solid Films* **411**, 152 (2002).
- ¹³D. L. Young, D. L. Williamson, and T. J. Coutts, *J. Appl. Phys.* **91**(3), 1464 (2002).
- ¹⁴Y. Sato, J. Kiyohara, A. Hasegawa, T. Hattori, M. Ishida, N. Hamada, N. Oka, and Y. Shigesato, *Thin Solid Films* **518**(4), 1304 (2009).
- ¹⁵J. H. Ko, I. H. Kim, D. Kim, K. S. Lee, T. S. Lee, J. H. Jeong, B. Cheong, Y. J. Baik, and W. M. Kim, *Thin Solid Films* **494**(1-2), 42 (2006).
- ¹⁶S. Venkataraj, S. Hishita, Y. Adachi, I. Sakaguchi, K. Matsumoto, N. Saito, H. Haneda, and N. Ohashi, *J. Electrochem. Soc.* **156**(6), H424 (2009).
- ¹⁷S. Aksoy, Y. Caglar, S. Ilican, and M. Caglar, *Opt. Appl.* **40**(1), 7 (2010).
- ¹⁸E. López-Ponce, J. L. Costa-Krämer, M. S. Martín-González, F. Briones, J. F. Fernández, A. C. Caballero, M. Villegas, and J. de Frutos, *Phys. Status Solidi A* **203**(6), 1383 (2006).
- ¹⁹J. H. Ko, I. H. Kim, D. Kim, K. S. Lee, T. S. Lee, B. Cheong, and W. M. Kim, *Appl. Surf. Sci.* **253**(18), 7398 (2007).
- ²⁰J. J. Rehr and R. C. Albers, *Rev. Mod. Phys.* **72**(3), 621 (2000).
- ²¹D. E. Proffit, Q. Ma, D. B. Buchholz, R. P. H. Chang, M. J. Bedzyk, T. O. Mason, and N. J. Dudney, *J. Am. Ceram. Soc.* **95**(11), 3657 (2012).
- ²²T. Eguchi, H. Inoue, A. Masuno, K. Kita, and F. Utsuno, *Inorg. Chem.* **49**(18), 8298 (2010).
- ²³K. Nomura, T. Kamiya, H. Ohta, T. Uruga, M. Hirano, and H. Hosono, *Phys. Rev. B* **75**(3), 035212 (2007).
- ²⁴D.-Y. Cho, J. Song, K. D. Na, C. S. Hwang, J. H. Jeong, J. K. Jeong, and Y.-G. Mo, *Appl. Phys. Lett.* **94**(11), 112112 (2009).
- ²⁵V. Petkov, *J. Appl. Crystallogr.* **22**, 387 (1989).
- ²⁶N. G. Alexandropoulos, M. J. Cooper, P. Suortti, and B. T. M. Willis, in *International Tables for Crystallography* (John Wiley & Sons, Hoboken, NJ, 2006), Vol. C, pp. 653.

- ²⁷D. Waasmaier and A. Kirfel, *Acta Crystallogr., Sect. A: Cryst. Phys., Diff., Theor. Gen. Crystallogr.* **51**, 416 (1995).
- ²⁸B. Ravel and M. Newville, *J. Synchrotron Radiat.* **12**(Pt. 4), 537 (2005).
- ²⁹Y. Joly, *Phys. Rev. B* **63**(12), 125120 (2001).
- ³⁰C. L. Farrow, P. Juhas, J. W. Liu, D. Bryndin, E. S. Bozin, J. Bloch, T. Proffen, and S. J. Billinge, *J. Phys. Condens. Matter* **19**(33), 335219 (2007).
- ³¹See supplementary at <http://dx.doi.org/10.1063/1.4861378> for more details.
- ³²Q. Zhu, Q. Ma, D. B. Buchholz, R. P. H. Chang, M. J. Bedzyk, and T. O. Mason, *Appl. Phys. Lett.* **103**, 031913 (2013).
- ³³Y. Jeong, C. Bae, D. Kim, K. Song, K. Woo, H. Shin, G. Cao, and J. Moon, *ACS Appl. Mater. Interfaces* **2**(3), 611 (2010).
- ³⁴D. Shiri, Y. Kong, A. Buin, and M. P. Anantram, *Appl. Phys. Lett.* **93**(7), 073114 (2008).
- ³⁵R. G. Goodchild, J. B. Webb, and D. F. Williams, *J. Appl. Phys.* **57**(6), 2308 (1985).
- ³⁶X. Liu, J. Iqbal, Z. Wu, B. He, and R. Yu, *J. Phys. Chem. C* **114**, 4790 (2010).
- ³⁷J. Robertson, *Phys. Status Solidi B* **245**(6), 1026 (2008).
- ³⁸M. Orita, H. Ohta, M. Hirano, S. Narushima, and H. Hosono, *Philos. Mag. B* **81**(5), 501 (2001).
- ³⁹Z. Liu, K. Handa, K. Kaibuchi, Y. Tanaka, and J. Kawai, *J. Electron Spectrosc. Relat. Phenom.* **135**(2-3), 155 (2004).
- ⁴⁰M. S. Moreno, A. Varela, and L. C. Otero-Diaz, *Phys. Rev. B.* **56**(9), 5186 (1997).